

# The correlation between Rare Earth Elements and tin in granite, quartz vein, and weathered granite samples, in South Bangka, Bangka Belitung Islands, Indonesia

ARMIN TAMPUBOLON<sup>1,2,\*</sup>, ILDREM SYAFRI<sup>1</sup>, MEGA FATIMAH ROSANA<sup>1</sup>, EUIS TINTIN YUNINGSIH<sup>1</sup>

<sup>1</sup> Faculty of Geological Engineering, Padjadjaran University, Dipati Ukur Street No. 35, Bandung 40132, West Java, Indonesia

<sup>2</sup> Research Centre for Geological Resources, National Research and Innovation Agency, Sangkuriang Street No. 21, Bandung 40135, West Java, Indonesia

\* Corresponding author email address: [armin.tampubolon@gmail.com](mailto:armin.tampubolon@gmail.com)

**Abstract:** The presence of Rare Earth Elements (REEs) is often correlated with tin (Sn), particularly at placer deposits in the Bangka Belitung Islands. However, there is limited information on the correlation between Sn and REEs. Therefore, this study aimed to investigate the correlation between REEs and Sn using data analysis of Sn-W, REEs, Y, Th, and U in granite, quartz veins, and weathered granite samples from South Bangka. The statistical analysis carried out using the Pearson correlation coefficient and multivariate processing showed that Sn-REEs have a weakly negative correlation. The examination of genetic aspects through chemical analysis, mineralogy, and Scanning Electron Microscope (SEM) data, showed that Sn and REE originated from the same magmatic fluids but different depositional phases due to magmatic-hydrothermal processes. The results show that REEs were formed during the early magmatic crystallization as mineral and stannite (Cu-Sn) in granite, while Sn was enriched as cassiterite in the deposition of late-stage hydrothermal fluid in parental granite. Moreover, the variation in deposition stage and temperature during the formation process is depicted in statistically uncorrelated values for Sn and REEs.

**Keywords:** Sn-REEs, stannite, cassiterite, Pearson coefficient, multivariate, genetic relationship

## INTRODUCTION

Rare Earth Elements (REEs) are significantly crucial in various high-technology applications such as computers, cellular phones, TVs, laser beams, missile weapons, and electric vehicles. In the 21st century era of advanced technology, REEs are recognized as essential environmentally friendly future energy raw materials (Weng *et al.*, 2017) due to the significance for clean energy and the associated supply risks (George *et al.*, 2015).

Previous studies have established that REEs can occur in various types of deposits (Murakami & Ishihara, 2008; Chengyu, 2008; Weng *et al.*, 2013). In Indonesia, REEs are associated with secondary/placer tin deposits (Abidin, 1999; Soetopo, 2013) or as a by-product of placer tin mining in the form of monazite, zircon, and xenotime grains on Bangka-Belitung Island (Zglinicki *et al.*, 2021). These elements are also associated with cassiterite originated from various types of primary tin deposits in granite and meta-sedimentary through erosion processes, which are re-deposited as placer tin during the Neogene - Quaternary period (Schwartz & Surjono, 1991). Indications of REEs primary deposits connected to cassiterite accessories include

monazite, xenotime, and zircon in granite pegmatite veins on the Menumbing-Bangka, Karimun, and Kundur Tin Belt (Mesker, 2013). Furthermore, some deposits were found along with tin anomalies in quartz veins in weathered granite bodies in Bangka.

The formation of REEs in hydrothermal systems is influenced by various conditions, including a decrease in pH, dominant magmatic or meteoric composition, a chloride-rich complex, and a change in alkalinity (Franco, 1992), suggesting that hydrothermal Sn carriers also precipitate REEs. Based on previous investigations, the total REE content of Bangka granite was found to be more than 200 ppm, while 649 ppm was discovered in the Toboali area. Additionally, it was discovered that REEs enrichment occurs in the C horizon weathered granite (Shita & Lucas, 2009).

In South Bangka, primary and secondary REEs are showed in veins hosted in biotite granite, featuring alteration containing quartz, apatite, zircon, and pyrite. Furthermore, there is alluvial REEs deposits, originating from granite containing cassiterite, monazite, zircon, xenotime, ilmenite, and apatite (Abidin *et al.*, 2014), which suggests REEs enrichment. This phenomenon shows the role of late-stage

hydrothermal (Camilla *et al.*, 2019), and primary REEs resulting from the heavy enrichment process (Ng *et al.*, 2017).

A common perception suggests that REEs are formed simultaneously with Sn, serving as an indicator of REEs. However, study focusing on the spatial relationship between the two elements is limited. Therefore, this study aimed to investigate Sn-REEs correlation, discussing possible genetic relationship.

## GEOLOGY

Bangka Island, known as Tin Island, is part of the Southeast Asian tin belt, covered by an extensive granite rock as a member of the Triassic-Jurassic-Jurassic Kelabat Granite. This granite consists of Type-I and Type-IS (Crow & Van Leeuwen, 2005), intruding the Pemali Complex composed of phyllites, schists, and gneiss of the Permo-Carbon age. The Tanjung Genting Formation is composed of alternating metasediments of claystone, siltstone, and sandstone of Triassic (Mangga & Djamal, 1994; Margono *et al.*, 1995), as shown in study areas of South Bangka, presented in Figure 1. Moreover, this island has been recognized as a tin-producing area since the 17th Century.

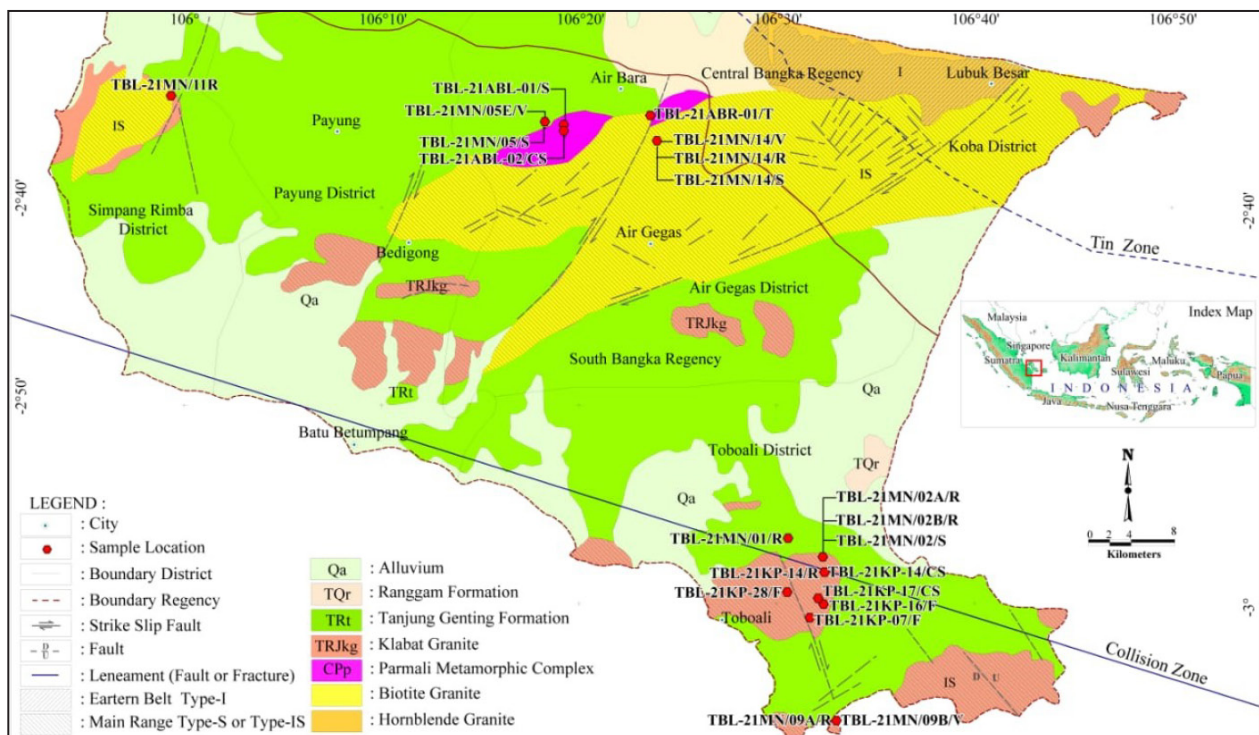
The Southeast Asian tin belt is one of the largest tin-producing areas globally, consisting of granite provinces such as Eastern (East Malaya), Main Range (South Thailand - West Malaya), Northern (North Thailand), and Western (Southwest Thailand-East Myanmar) (Cobbing *et al.*, 1992). The N-S Palaeo-Tethys Bentong-Raub suture line divides

Peninsular Malaysia into the Sibumasu Block in the west and the Indochina Block in the east, which traverses the eastern part of Bangka Island in the Bangka-Belitung Sea, and not exposed on land (Hutchison, 2014).

The types of granite in the study area include dominant biotite and hornblende, which occupies the central and southwest parts, respectively, as shown in Figure 1. The Permo Triassic Klabat granite occupies West, South, Central, and East Bangka, with lithology comprising granite, granodiorite, diorite, as well as S-type and I-type quartz diorite (Kurnia & Priadi, 2013; Kurniawan, 2014; Ng *et al.*, 2017). The Main Range granite province is the primary source of Sn-W mineralization and is known as the tin zone (Schwartz *et al.*, 1995; Crow & Van Leeuwen, 2005). The study area of South Bangka is within the S or IS-granite types of the Main Range (Crow & Van Leeuwen, 2005). Based on the investigation, S-type granite magma originating from sedimentary protoliths is suitable for Sn mineralization (Liu *et al.*, 2020).

Referring to research data at the Pemali Mine, Central Bangka, tin mineralization was found in Triassic granite pluton rocks, where the magmatic evolution process declined from medium to coarse-grained biotite granite, mega crystal medium-grained, and muscovite/two mica granite (Schwartz *et al.*, 1995). Meanwhile, tin mineralization is limited to two-mica granite, where cassiterite is disseminated or in the form of veins in greisen (Schwartz & Surjono, 1991).

Various metallic minerals such as base metals (Cu, Pb, Zn), Li, W, REEs (as zircon, monazite, and xenotime



**Figure 1:** Geology of the South Bangka and locations of rock sampling (modified from Crow & Van Leeuwen, 2005; Hutchison, 2014).

inclusions in granite), ilmenite, rutile, magnetite, and iron have also been found in tin deposits, categorized as polymetallic deposits. Primary polymetallic tin deposits were found in South Bangka in the form of quartz veins containing cassiterite, tungsten, zinc oxide, and ilmenite (Reza *et al.*, 2018; Franto *et al.*, 2019).

The presence of REEs in tin-bearing granite, such as Klabat Granite or other plutons as part of the Main Range, particularly from S or IS-types, is significantly common on Bangka Island (Crow & Van Leeuwen, 2005). The available data also show that REEs content in Bangka granite is significant, reaching 200 ppm in the Toboali area, and 640 ppm locally (Shita & Lucas, 2009).

### ANALYTICAL METHODS

In this study, inductively coupled plasma mass spectrometry (ICP-MS) was applied to analyze REE, Y, Sn, W, Th, and U contents of all samples from the study areas at Intertek Laboratory Jakarta, Indonesia. The analysis applied ICP-MS determination with acid digestion in Teflon tubes. Initially, samples were dried, crushed by a jaw crusher or iron mortar, and ground using a mill. A solution of rock samples for ICP-MS analyses was made by acid digestion of fused glass beads using lithium metaborate and tetraborate as flux. Subsequently, the laboratory instrument used was ICP-MS Agilent type 7700. Petrographic and microscopic descriptions of ore were carried out at the Laboratory of the Centre for Mineral Coal and Geothermal Resources, Geological Agency of Indonesia.

X-ray diffraction (XRD) was performed at the Laboratory of the Centre for Geological Survey, Geological Agency of Indonesia, and Laboratory Wuhan Centre, China Geological Survey (CGS). The main XRD instrument used was a PANalytical X'Pert PRO with a type series of PW3040/x0 X'Pert PRO, made in Nederland. A Cu-tube with a spinning or sample holder was used for the total test of the sample materials. The measurement angle (2-theta) applied was approximately 30 – 600, and agate grinders were used with grain sizes ranging from 5 – 10 µm or approximately 200 mesh.

Scanning Electron Microscope-Energy Dispersive (SEM-EDX) or Energy Dispersive X-ray Spectroscopy (SEM-EDS) instruments applied for analysis were of type JEOL JED-2200 Series (SEM JEOL-JSM6360LA). These analyses were performed at the Laboratory of the Centre for Geological Survey, Geological Agency of Indonesia in Bandung. The chemical compositions of minerals were measured using a Shimadzu electron probe microanalyzer (EPMA) 1600 at the laboratory of Wuhan Center, CGS, China. Simultaneously, backscattered electron (BSE) images were taken. During quantitative analysis, the operating conditions included 15 kV accelerating voltage, 10 nA beam current, and 1 µm beam diameter. Minerals from the SPI Company of America were used as standards, and a program based on the ZAF procedure was applied for data correction.

Samples with location codes TBL-21MN/02B/R/S, TBL-21MN/14/R/S, TBL-21MN/05/R/S, TBL-21KP/16/R, and TBL-21KP/07/F have been analyzed in previous studies using the method described above (Tampubolon *et al.*, 2022).

## RESULT AND DISCUSSION

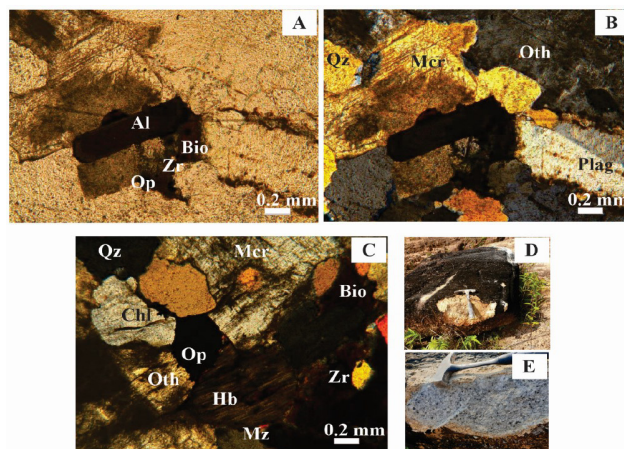
### Geochemical data

Granite samples were predominantly obtained from the Klabat granite rock formation in Toboali, while quartz vein and weathering samples were collected around the contact area of the Pemali Metamorphic Complex and granitoid rocks in Air Gegas, as shown in Figure 1. A total of 13 samples of granite/quartz veins and 23 weathered granite were analyzed using ICP-MS methods for Sn, W, REEs, Y, Th, and U, with the analysis results, presented in Table 1.

### MINERALOGY

#### Petrography and ore microscopy

The TBL-21MN/2B/R granite sample from Toboali Pluton showed colorless, holocrystalline, hypidiomorphic granular, fine grain size to approximately 8.0 mm, euhedral to anhedral crystals composed of quartz (35%), orthoclase (30%), plagioclase (5%), microcline (12%), hornblende (6%), biotite (4%), opaque minerals (2%), chlorite (1%), monazite (<1%), and zircon (<1%) (Figure 2). Based on the relationship between metallic minerals in the polished



**Figure 2:** Photomicrograph of thin section sample TBL-21MN/2B/R, Klabat Granite. A. Plane polarized light, showing biotite (Bio) with elongated blackish-brown of sub-euhedral crystal, allanite (Al) with euhedral elongated crystal, opaque minerals (Op), and fine grain of zircon (Zr) with bright yellow. B. Cross Nicol, showing microcline (Mcr) with irregular brownish-yellow crystal, plagioclase (Plag) with prismatic twin crystal, orthoclase (Oth) with pale gray, and quartz (Qz) with yellow anhedral crystal. C. Cross Nicol, showing quartz (Qz), microcline (Mcr), orthoclase (Oth), biotite (Bio), hornblende (Hb) with dark greenish-brown, chlorite (Chl) with blackish-white, zircon (Zr) with yellow sub-euhedral crystal, monazite (Mz) with bright pinkish-yellow, and opaque minerals has euhedral crystal. D. Boulder of mineralized granite from the basement of laterite profile. E. Sample of granite boulder consists of quartz, feldspar, biotite, and a little hornblende.



**Table 1:** Data analysis of Sn-W, REEs, Y, Th, and U in granite/quartz vein samples, and weathered granite (in ppm) (Tampubolon *et al.*, 2022).

Sample	Sample Code	Element																			ΣREE
		Sn	W	La	Ce	Pr	Nd	Sm	Eu	Gd	Tb	Dy	Ho	Er	Tm	Yb	Lu	Y	Th	U	
VEIN	TBL-21 MN 14/V	65.1	0.9	62.7	154	15.2	50.1	8	0.1	4	0.56	2	0.3	0.9	0.1	0.8	0.11	4.6	38.5	3.19	298.87
	TBL-21 MN 05 E/V	142	288	80.9	131	20.4	80.6	16.7	0.2	12.2	1.35	10.6	1.2	3.6	0.4	3.7	0.49	27.7	32.5	7.28	363.34
	TBL-21MN 09 B/V	3.91	0.88	1.18	2.47	0.28	1.13	0.48	0.02	0.58	0.22	1.89	0.44	1.37	0.25	1.1	0.23	13.5	5.97	1.77	11.643
	TBL-21 MN 14/R	22.5	1.7	74.5	201	15.8	58.1	10.8	0.1	6.5	0.68	2.7	0.4	0.9	0.2	0.9	0.12	7.1	44.1	3.7	372.7
GRANITE	TBL-21 KP 14/R	10.7	6.6	28	67.8	7.35	27	6.8	0.3	5.6	0.93	4.6	0.8	2.5	0.4	2.6	0.38	25.5	58.9	17.8	155.06
	TBL-21 KP 16/F	4.5	2.6	77.2	160	17.5	61.6	12.5	0.7	10.4	1.79	10.4	2.1	6.6	1	6.9	1.01	64.7	75.4	15.6	369.7
	TBL-21 KP-28/F	2.5	1.1	51	110	12.1	44	9	0.6	7.9	1.41	8.3	1.8	5.2	0.8	5.4	0.78	50.6	69.6	13.6	258.29
	TBL-21 KP 07/F	1.8	1.4	322	266	58.6	204	45.2	2.2	39.3	5.92	32.9	5.7	15.8	2.1	13.1	1.87	165	70.3	16.8	1014.7
	TBL-21 MN 11/R	4.1	8.1	37.5	78.8	9.04	31.9	6.9	0.7	5.4	0.83	4.4	0.8	2	0.3	1.9	0.33	20.2	28.7	9.13	180.8
	TBL-21MN 02 A/R	2.6	0.8	21.9	36.3	5.86	21.6	4.8	0.4	4.2	0.54	3.5	0.6	2.1	0.3	2.1	0.37	16.1	55.7	12.3	104.57
	TBL-21MN 02 B/R	2.6	0.99	222	437	54.6	220	53.7	2.8	51.3	7.65	39	6.3	15.7	2.2	12.7	1.65	163	52.9	11.4	1126.6
	TBL-21MN 01/R	6.6	6	99.8	213	23.6	85.5	16.7	1.3	10.5	1.55	7.4	1.2	3.3	0.5	3.1	0.43	25	51.7	3.54	467.88
	TBL-21 ABR/01/T	13.6	3.3	55.6	234	12.6	40.6	7.4	0.1	4.6	0.61	3	0.5	1.3	0.2	1.3	0.24	10.1	49.4	6.1	362.05
WEATHERED GRANITE	TBL-21KP 14/CS (0-0.7 m)	4.9	3.7	30.2	158	7.78	29.1	6.1	0.2	5.4	0.87	5.3	1	3.8	0.6	3.2	0.52	33.1	81.7	10.4	252.07
	TBL-21KP 14/CS (0.7-1.7 m)	4.9	3.6	33.4	142	8.22	30.2	6.3	0.3	4.7	0.72	4.3	0.8	2.3	0.4	2.5	0.38	21.1	76.7	9.93	236.52
	TBL-21KP 14/CS (1.7-5.5 m)	5.8	4.3	28.2	76.7	6.8	25.3	5.5	0.2	4.1	0.61	3.3	0.7	1.9	0.3	2.1	0.3	18.6	74.9	9.9	156.01
	TBL-21KP 14/CS (5.5-6.7 m)	9.5	3.2	31	136	8.09	29.6	6.1	0.1	4.3	0.55	2.5	0.6	1.2	0.2	1.3	0.21	12.2	64.7	8.62	221.75
	TBL-21 KP 17/CS (0-0.2 m)	6.2	2.9	34.6	68	8.02	28.5	5.8	0.4	4.4	0.74	4.1	0.8	2.4	0.4	2.5	0.38	19.7	37.9	9.27	161.04
	TBL-21 KP 17/CS (0.2-2.7 m)	7.3	3.4	46.9	79.9	9.6	33.9	7	0.6	5.4	0.81	4.9	0.9	2.7	0.4	2.9	0.4	26	46.5	12.3	196.31
	TBL-21 KP 17/CS (2.7-3.2 m)	17	3.5	35.1	36.4	6.67	22.2	4.1	0.3	3.4	0.54	2.9	0.6	1.6	0.2	1.6	0.24	17.1	15.2	2.55	115.85
	TBL-21 KP 17/CS (3.2-4.2 m)	7.4	2.5	93.2	70.4	14.7	52.7	9.2	0.8	7.8	1.17	6.6	1.4	4.4	0.6	4.1	0.62	46.9	26.3	4.8	267.69
	TBL-21 KP 17/CS (4.2-5.2 m)	10.4	1.6	38	59.2	7.79	27.2	5.2	0.4	4.3	0.64	3.5	0.7	2	0.3	2	0.3	18.7	19	3.42	151.53
	TBL-21 KP 17/CS (= 5.2 m)	2.4	2	121	158	24.4	87.9	17.4	1.3	14.4	2.32	12.9	2.5	6.9	1	6.6	0.94	66.8	71.4	10.4	457.56
	TBL-21 ABL 01/S (0-1 m)	19.1	23.3	56.3	175	15.5	53.9	111.5	0.1	7.2	1.03	4.8	1	3	0.4	3.3	0.52	23.9	75.5	8.25	433.55

Table 1: (Continued)

Sample	Sample Code	Element																			ΣREE
		Sn	W	La	Ce	Pr	Nd	Sm	Eu	Gd	Tb	Dy	Ho	Er	Tm	Yb	Lu	Y	Th	U	
WEATHERED GRANITE	TBL-21 ABL 01/S (1-2 m)	18.8	30.9	44.3	162	12.7	43.1	9.1	0.1	5.7	0.87	4.8	1	2.9	0.5	3	0.38	20.9	67.8	7.55	290.45
	TBL-21 ABL 01/S (2-3 m)	14.2	33.1	21.5	124	6.17	20.7	5.1	0.1	3.9	0.63	3.6	0.9	2.3	0.4	3.1	0.45	18.6	54.3	11.3	192.85
	TBL-21 ABL 01/S (3-4 m)	15.4	23.6	29.1	124	8.6	29.2	7.1	0.1	4.8	0.88	5.6	1.2	3.6	1	4.2	0.62	33.4	70.2	19.1	220
	TBL-21 ABL 02/CS	39.7	4.6	75.9	174	18.6	61.6	15.3	0.1	9.2	1.18	6.2	1.1	3.2	0.5	3.4	0.52	30.5	48.8	14.4	370.8
	TBL-21 MN 02/S (0-3 m)	102	96.2	63.8	65.2	11	29	4.2	0.9	4.3	0.59	3.5	0.7	2.6	0.4	2.8	0.46	20.9	67.9	4.76	189.45
	TBL-21 MN 02/S (3-6m)	93	45.8	93.8	73.6	14.9	35.6	4.2	1	3.5	0.58	2.9	0.6	1.9	0.3	1.9	0.46	14.2	53.2	3.6	235.24
	TBL-21 MN 05/S (0-4 m)	22.1	8.3	60.6	169	16.6	54.1	11.2	0.1	7.8	0.97	4.3	0.8	2.1	0.3	2.3	0.39	14.8	75.9	6.99	330.56
	TBL-21 MN 05/S (4-8 m)	16.1	4.9	49	206	14	45.1	9.7	0.1	6.6	0.86	4	0.8	2.4	0.4	2.5	0.43	15	68.6	9.64	341.89
	TBL-21 MN 14/S (0-1.5 m)	26.9	7.1	37.9	92.4	8.05	28.3	4.5	0.1	2.8	0.35	2.3	0.5	1.5	0.2	1.6	0.2	9.7	67.2	3.54	180.7
	TBL-21 MN 14/S (1.5-2 m)	28.7	5.5	24.5	72	5.4	17.5	3	0.1	1.9	0.31	1.8	0.5	1.2	0.2	1.5	0.19	7.5	64.1	3.09	130.1
	TBL-21 MN 14/S (2-4 m)	22.3	6.5	68.2	152	14.4	45	7.3	0.1	4.1	0.7	3.7	0.8	2.5	0.3	2.5	0.35	15.7	90	3.96	301.95
	TBL-21 MN 14/S (4-5.5 m)	12.4	13.4	84.5	257	17.7	65.1	10	0.1	5.6	0.72	3.6	0.8	2.5	0.4	2.2	0.37	15.8	101	5.4	450.59

section as shown in Figure 3, the formation sequence is the stages I, II, and III, consisting of pyrite, magnetite, and sphalerite, while stage IV comprised chalcopyrite and stannite, respectively. Compared to the observations under the thin section, monazite is not present in the polished section.

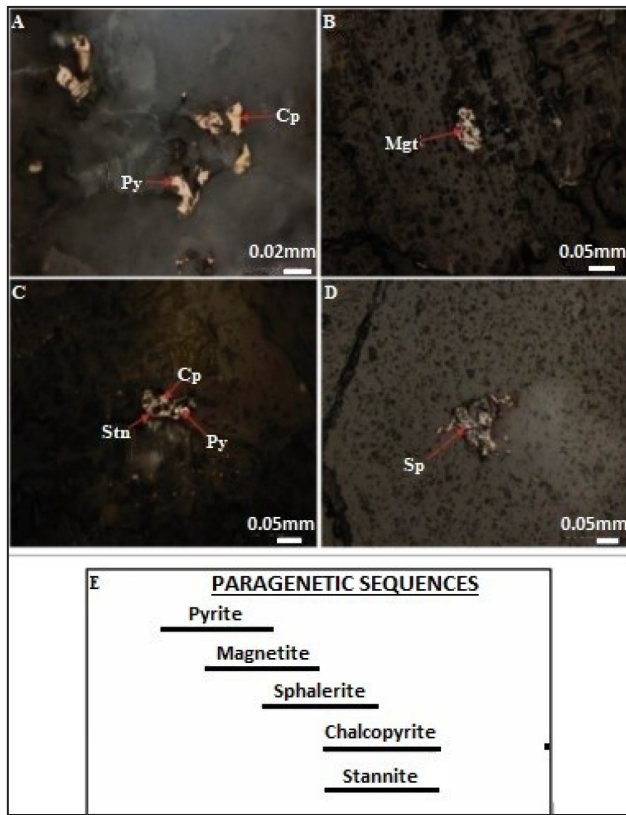
The petrographic description of the quartz vein hosted in the granite sample (TBL-21MN/5E/R) showed a colorless, holocrystalline, hypidiomorphic granular texture, fine grain size of approximately 6.0 mm, subhedral to anhedral crystals composed of quartz (50%), orthoclase (17%), opaque (22%), ore minerals (10%), and monazite (<1%), as shown in Figure 4. However, monazite was not observed in the polished section except cassiterite and hydrous iron oxide, as presented in Figures 4D and 4E. Based on Figure 5, as showed by the polished section of the quartz vein hosted in granite, REEs mineral was not observed on the thin section of sample TBL-21MN/14/R.

## XRD

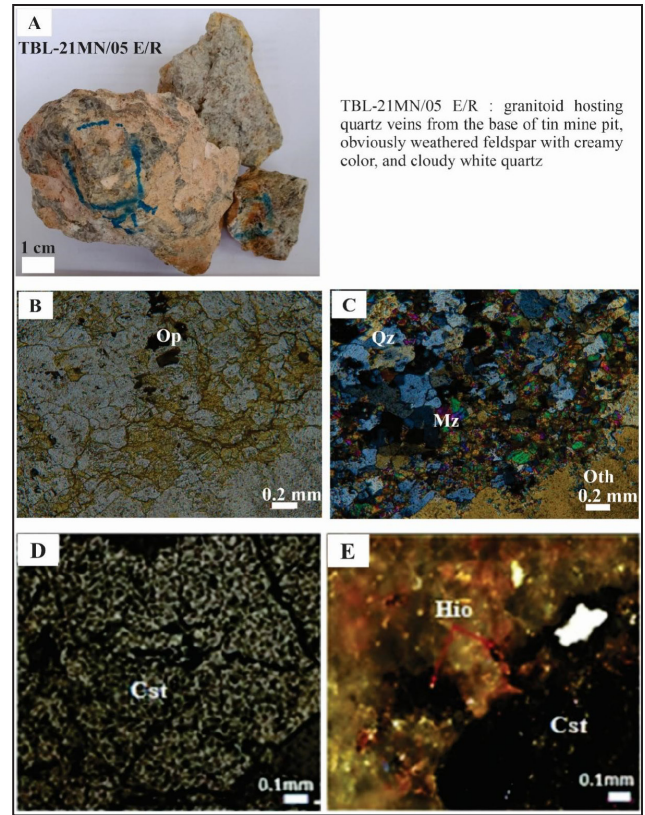
A total of three samples were taken from a weathering profile in the Toboali Area for mineralogical composition analysis using the XRD method at the Geological Survey Central Laboratory (PSG) of the Geological Agency. The results presented in Table 2 show that one of the weathering samples showed the presence of cassiterite together with gibbsite in the upper horizon weathering profile sample TBL-21MN/02/S (0-3 m). However, in the bedrock sample (TBL-21MN/02B/R) presented in Figure 3C, cassiterite was not observed, except for stannite.

## SEM and EPMA

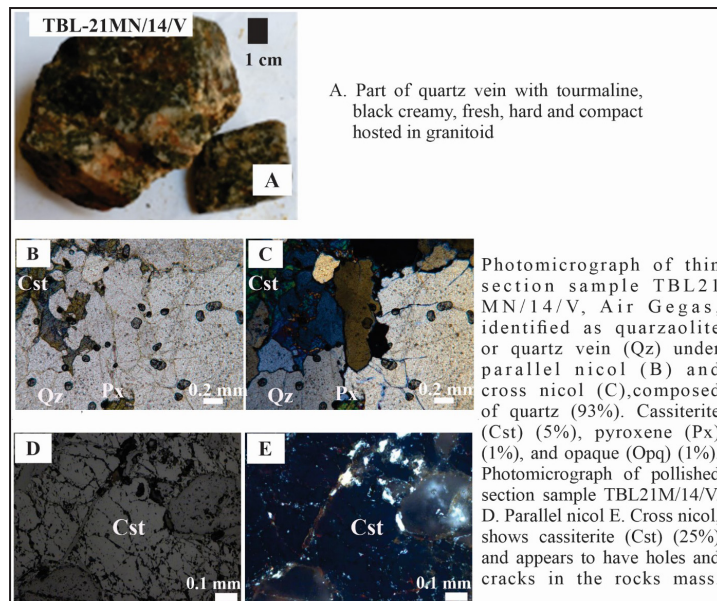
After several analyses using SEM-EDS and EPMA elemental mapping, some samples showed the presence of tin and REEs in quartz veins hosted in granite, namely TBL-21MN/05E/R (Air Gegas) and TBL-21MN/09A/R (Toboali), as presented in Figures 6, 7 and 8. The weathering



**Figure 3:** Photomicrograph of a polished section of the granite rock sample TBL-21MN/02B/R, Toboali, consisting of pyrite (Py) 2%, and chalcopyrite (Cp) < 0.5% (A), magnetite (Mgt) (trace) (B), stannite (Stn) (< 0.5%), chalcopyrite < 0.5%, and pyrite (C), sphalerite (Sp) (trace) (D). It appears that chalcopyrite and stannite are intergrowths.


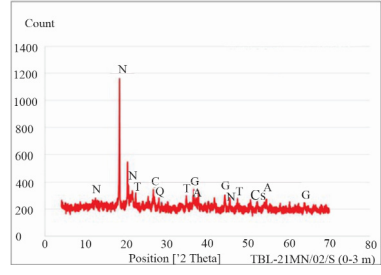

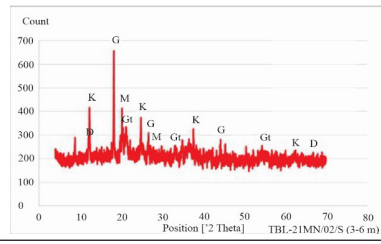
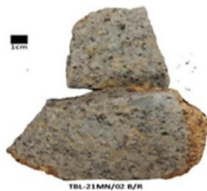
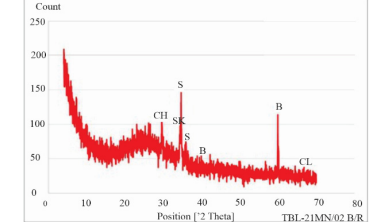


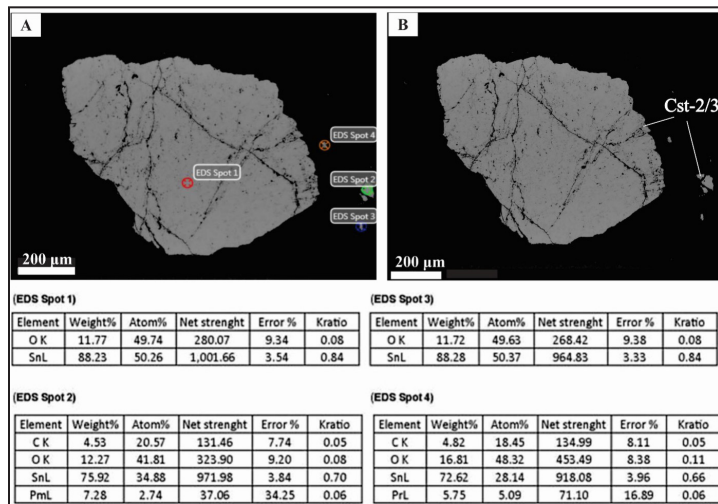
**Figure 4:** Mineralized quartz vein hosted in granite of sample TBL-21MN/05E/R, Air Gegas, from tin mine pit (A). B. Plane polarized light showing opaque minerals (Op) with black sub-euhedral crystals. C. Cross Nicol shows bluish-black crystals (Qz) and pinkish-yellow monazite grains (Mz). D. Plane polarized of polished section showing grey cassiterite with cracks (Cst) (20%). E. Cross Nicol of the polished section with the presence of hydrous iron oxide (Hio) (3%) and cassiterite (Cst).



**Figure 5:** Photomicrograph of thin and polished sections of quartz vein sample in granitoid (TBL-21MN/14/R), Air Gegas.

**Table 2:** XRD results of weathered granite samples from laterite profile (TBL-21MN/02/R/S), Toboali. G = Gibbsite, Q = Quartz, C = Cristobalite, N = Nacrite, T = Tourmaline, Cs = Cassiterite, A = Anatase, K = Kaolinite, M = Muscovite, D = Dickite, G = Geothite, S = Spinel, B = Brucite, C = Calcite, CH = Chalcopyrite, SK = Skutterudite.

Sample	Compound Name	Chemical Formula	Diffractogram
 <b>TBL-21MN/02/S (0-3 m)</b>	Gibbsite (50%)	$\text{Al}(\text{OH})_3$	
	Quartz (11%)	$\text{SiO}_2$	
	Cristobalite (15%)	$\text{SiO}_2$	
	Nacrite (10%)	$\text{Al}_2\text{SiO}_5(\text{OH})_4$	
	Tourmaline (13%)	$\text{H}_8\text{Na}_2(\text{Mg}, \text{Fe})_6\text{B}_3\text{Al}_{12}\text{Si}_{12}\text{O}_{62}$	
	Cassiterite (9%)	$\text{SnO}_2$	
	Anatase (4%)	$\text{TiO}_2$	
 <b>TBL-21MN/02/S (3-6 m)</b>	Gibbsite (38%)	$\text{Al}(\text{OH})_3$	
	Kaolinite (25%)	$\text{Al}_2(\text{Si}_2\text{O}_5)(\text{OH})_4$	
	Muscovite (16%)	$(\text{K}, \text{Na})(\text{Al}, \text{Mg}, \text{Fe})_2(\text{Si}_{3.1}\text{Al}_{0.9})\text{O}_{10}(\text{OH})_2$	
	Dickite (19%)	$\text{Al}_2\text{Si}_2\text{O}_5(\text{OH})_4$	
	Geothite (17%)	$\text{Fe}_{+3}\text{O}(\text{OH})$	
 <b>TBL-21MN/02 B/R</b>	Spinel (18%)	$(\text{Mn}_{0.469}\text{Fe}_{0.651}\text{Ti}_{0.88}((\text{Ti}_{0.12}\text{Fe}_{0.511}\text{Mn}_{0.369})\text{O}_4))$	
	Brucite (6%)	$\text{Mg}(\text{OH})_2$	
	Calcite (6%)	$\text{CaCO}_3$	
	Chalcopyrite (9%)	$\text{CuFeS}_2$	
	Skutterudite (20%)	$\text{CoAs}_3$	



**Figure 6:** A. Photomicrographs of SEM-EDS with observation spots. B. BSE image and four tables of SEM-EDS mapping results for Sn and other elements for each sample spot of TBL-21MN/05E/R. The sample refers to Figure 4. Cst 2/3 = cassiterite

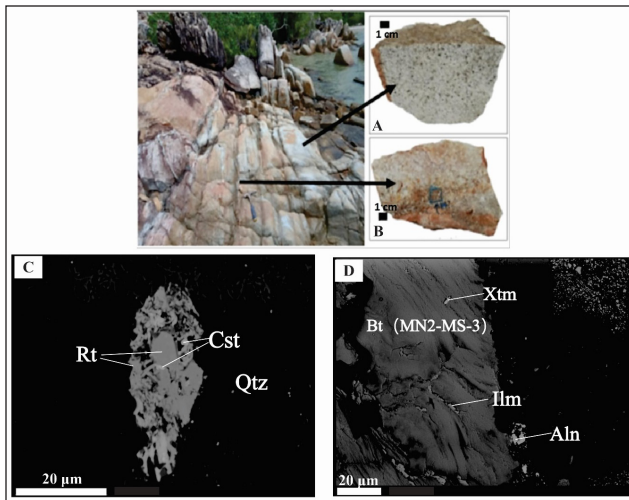
of granite (TBL-21ABL 02/CS), based on SEM-EDS mapping results, contained Sn, Pr, and Dy, as shown in Table 3 and Figure 9.

### Sn-REEs correlation in granite and quartz vein samples

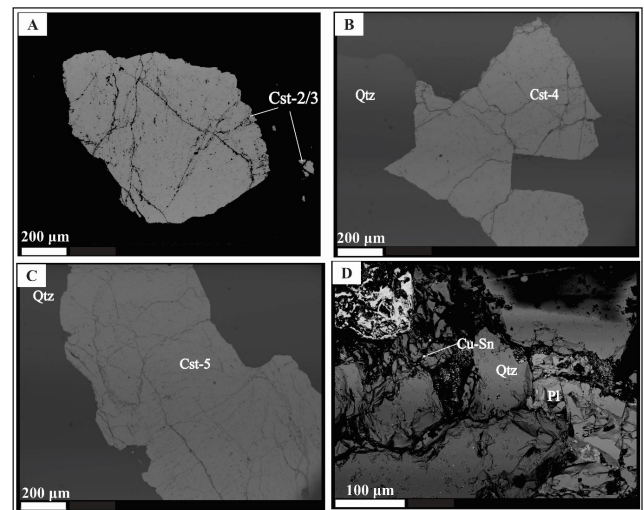
The relationship between Sn and REEs was assessed using a bivariate statistical approach to calculate the Pearson

correlation with ICP data of granite and quartz veins from Table 1. The results of bivariate processing showed that the Pearson correlation value in Table 5 ranged from +1 to -1. A +1 value indicated a strong positive correlation, while  $< +1$  and  $> 0.5$  was categorized as a moderate positive correlation. When the value is -1, it indicates a strong negative correlation, while -0.5 to  $< -1$  represents a weak to moderate negative correlation.





**Figure 7:** Outcrop of granite harboring quartz veins in Toboali, 5-10 cm thick, strike/dip N 155° E/80°. A. Granite has medium grain texture, light grey, consisting of quartz, feldspar, and biotite (TBL-21MN/09A/R). B. Quartz vein sample, grey-yellow, massive, compact, metallic sulfide, and iron oxide (TBL-21MN/09B/R). C. BSE image of granite sample TBL-21MN/09A/R containing xenotime (Xtm), ilmenite (Ilm), and allanite (Aln) in biotite (Bt)). D. BSE image of quartz sample TBL-21MN/09B/R containing ilmenite (Rt) and cassiterite (Cst).



**Figure 8:** BSE image of quartz vein sample (TBL-21MN/05E/R) and (TBL-21MN/14/R), Air Gegas, hosted in granite. A. Sub-rounded cassiterite crystal (Cst 2/3). B. Irregular crystal of cassiterite (Cst-4) set in quartz vein (Qtz) with a table of EPMA analysis results. C. Elongated crystal of cassiterite (Cst-5). D. BSE image of quartz veins (Qtz) (TBL-21MN/14/R) showing Cu-Sn grain in crushed quartz veins, with quartz (Qtz) and plagioclase (Pl) as rock-forming minerals.

**Table 3:** The results of SEM-EDS mapping on sample TBL-21ABL 02/CS, Air Gegas, and two mapping spots referring to Figure 9C.

(REES-4)

Element	Weight (%)	Atom (%)	Net Strenght	Error (%)	Kratio
SrL	5.41	2.64	68.05	10.09	0.05
Y L	14.88	7.17	160.25	9.22	0.13
P K	61.81	85.47	1,193.05	3.78	0.57
DyL	17.91	4.72	30.29	31.74	0.13

(EDS Spot 5)

Element	Weight (%)	Atom (%)	Net Strenght	Error (%)	Kratio
O K	38.47	67.43	463.09	10.36	0.09
SrL	1.78	0.57	43.11	10.46	0.01
SnL	2.14	0.50	37.87	23.59	0.02
TiK	51.84	30.35	988.81	2.69	0.47
PrL	5.77	1.15	32.69	24.81	0.04

From the data processing using the SPSS 26 program, the results showing high to moderate correlation values were shown with a yellow color, as shown in Table 4. Based on the Pearson correlation value, it was discovered that Sn did not correlate with REEs, but was connected to W and Th.

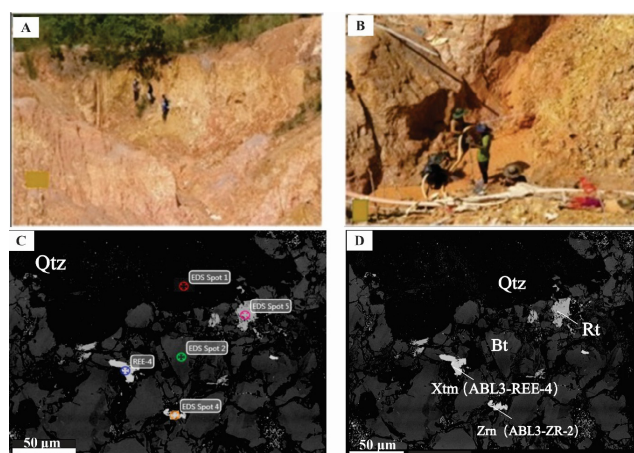
Applying the multivariate statistical method, the data collected from granite and quartz vein samples were

grouped into two components based on negative or positive correlation values that must be close to 1.0. The group of REEs data was determined to be positively correlated as component 1. Meanwhile, U and Th were assessed to component 2, and Sn-W as component 3, as shown in Table 4. The results of multivariate processing showed that Sn did not correlate with REEs in granite and quartz vein samples.



**Table 4:** The calculation results of the Pearson correlation of Sn, W, REEs, Y, Th, and U in rock/quartz veins and weathering samples. The yellow highlighted shows moderately positive or negative (\*) to strong correlation values (\*\*).

Sn	.900**	-0.137	-0.142	-0.102	-0.085	-0.117	-0.377	-0.161	-0.223	-0.162	-0.255	-0.252	-0.309	-0.249	-0.282	-0.280	-0.558	-0.390
W	1	-0.058	-0.135	-0.022	0.006	-0.007	-0.208	-0.036	-0.096	-0.013	-0.104	-0.093	-0.145	-0.072	-0.096	-0.124	-0.430	-0.164
La		1	.743**	.980**	.954**	.931**	.842**	.901**	.897**	.906**	.906**	.909**	.888**	.880**	.875**	.906**	0.322	0.258
Ce			1	.828**	.849**	.841**	.734**	.822**	.811**	.773**	.750**	.706*	.711**	.663*	.621*	.702*	0.122	-0.123
Pr				1	.994**	.981**	.893**	.957**	.950**	.952**	.940**	.930**	.913**	.899**	.879**	.924**	0.267	0.207
Nd					1	.995**	.908**	.977**	.967**	.967**	.948**	.932**	.918**	.900**	.874**	.925**	0.236	0.197
Sm						1	.926**	.993**	.985**	.983**	.964**	.945**	.934**	.913**	.886**	.940**	0.240	0.249
Eu							1	.933**	.947**	.932**	.938**	.922**	.927**	.899**	.883**	.918**	0.335	0.337
Gd								1	.996**	.993**	.977**	.958**	.950**	.928**	.902**	.955**	0.267	0.315
Tb									1	.994**	.988**	.971**	.968**	.945**	.923**	.970**	0.324	0.362
Dy										1	.992**	.982**	.974**	.963**	.943**	.979**	0.333	0.397
Ho											1	.996**	.993**	.982**	.970**	.995**	0.424	0.458
Er												1	.997**	.994**	.987**	.999**	0.479	0.509
Tm													1	.994**	.987**	.997**	0.516	0.524
Yb														1	.996**	.991**	0.538	0.558
Lu															1	.985**	0.572	.596*
Y																1	0.481	0.525
Th																	1	.703*
U																		1
Sn	.822**	0.281	-0.239	0.120	-0.105	-0.237	0.344	-0.217	-0.250	-0.262	-0.284	-0.207	-0.197	-0.188	-0.027	-0.247	0.004	-0.307
W	1	0.121	-0.140	0.019	-0.142	-0.236	0.277	-0.183	-0.176	-0.158	-0.138	-0.054	0.023	0.014	0.112	-0.119	0.128	-0.109
La		1	0.259	.905**	.842**	.646**	.655**	.693**	.672**	.618**	.604**	.620**	0.367	.539**	.638**	.564**	0.091	-0.160
Ce			1	.563**	.618**	.631**	-0.376	.443*	0.344	0.253	0.251	0.247	0.243	0.225	0.252	0.080	.708**	0.307
Pr				1	.968**	.871**	0.372	.831**	.769**	.676**	.650**	.638**	.428*	.589**	.660**	.532**	0.277	0.055
Nd					1	.930**	0.304	.890**	.831**	.748**	.728**	.703**	.486*	.647**	.670**	.611**	0.291	0.123
Sm						1	0.139	.939**	.870**	.790**	.757**	.708**	.553**	.699**	.685**	.641**	0.222	0.379
Eu							1	0.399	.482*	.526**	.504*	.533**	0.335	.469*	.551**	.591**	-0.287	-0.158
Gd								1	.970**	.918**	.886**	.846**	.653**	.822**	.817**	.814**	0.096	0.346
Tb									1	.980**	.963**	.926**	.759**	.908**	.889**	.899**	0.070	0.373
Dy										1	.986**	.966**	.833**	.951**	.911**	.952**	0.041	.419*
Ho											1	.969**	.850**	.965**	.914**	.953**	0.056	0.401
Er												1	.881**	.971**	.945**	.967**	0.088	0.385
Tm													1	.912**	.887**	.851**	0.136	.644**
Yb														1	.958**	.941**	0.079	.502*
Lu															1	.907**	0.090	.469*
Y																1	-0.087	0.396
Th																	1	0.175
U																		1



**Figure 9:** A. Sample TBL-21ABL 01/S, Air Gegas, top weathered granite with blackish grey, 0-1 m depth (horizon O), red laterite 1-2 m depth (horizon A), yellow laterite 2-4 m depth (horizon B), and Sn-bearing weathered granite as basement mined by local people (horizon C). B. Sample TBL-21ABL 02/CS, Sn-bearing granite altered to kaolinite, the basement of weathering profile. C. Photomicrographs of SEM-EDS sample TBL-21ABL 02/CS with mapping spots. D. BSE image of sample TBL-21ABL 02/CS showing xenotime (Xtm) at spot REES-4. Zrn = zircon, Bt = biotite, Qtz = quartz.

### Sn-REEs correlation in weathering samples

Based on the SEM-EDS results presented in Figure 9C, tin was detected along with REEs (Pr) in spot 5 SEM analysis of the TBL-21ABL-02/CS sample. Furthermore, Air Gegas, interpreted as the mineral composition of rutile (Rt) in the biotite fragment (Bt), as shown in Figure 9D. The results of the ICP analysis on weathering samples showed that the value of Sn content was small, where a significant value (102 ppm) was only obtained in sample TBL-21MN/02/S (0-3m) on the weathering profile of the Sn mine excavation in the Air Gegas Area, as shown in Table 1.

The relationship of Sn to REEs was determined using a bivariate statistical approach to calculate the Pearson correlation. The results of bivariate statistics using the SPSS 26 program yielded the Pearson correlation coefficient as shown in Table 4. The yellow color showed the magnitude of the correlation value according to numbers above 0.5, where values close to +1 and -1 were categorized as strongly positive and negative correlations, respectively. Correlation values of approximately -0.5 or +0.5 were classified as moderately negative and positive correlated, respectively. The total Pearson correlation value showed that Sn and REEs were far from +1 and -1, indicating the absence

**Table 5:** The calculation results of the multivariate correlation of Sn, W, REEs, Y, Th, and U in rock/quartz vein and weathering samples, the yellow color shows the correlation value of the components.

Element	Rock Sample			Weathering Sample			
	Component			Component			
	1	2	3	1	2	3	4
Sn	-0.075	-0.215	0.951	-0.224	0.109	-0.101	0.919
W	0.002	-0.042	0.978	0.026	-0.101	0.056	0.948
La	0.925	0.187	0.004	0.285	0.886	-0.107	0.263
Ce	0.860	-0.098	-0.076	0.094	0.414	0.852	-0.172
Pr	0.970	0.139	0.033	0.327	0.901	0.219	0.100
Nd	0.983	0.117	0.050	0.394	0.873	0.247	-0.093
Sm	0.986	0.133	0.026	0.511	0.705	0.319	-0.242
Eu	0.916	0.199	-0.207	0.412	0.392	-0.616	0.405
Gd	0.977	0.166	-0.012	0.663	0.678	0.091	-0.177
Tb	0.969	0.202	-0.071	0.776	0.590	0.010	-0.160
Dy	0.963	0.244	0.007	0.858	0.476	-0.047	-0.137
Ho	0.942	0.303	-0.081	0.867	0.447	-0.041	-0.131
Er	0.919	0.367	-0.065	0.883	0.419	-0.030	-0.032
Tm	0.908	0.377	-0.122	0.949	0.083	0.134	0.025
Yb	0.884	0.432	-0.047	0.935	0.314	0.018	0.003
Lu	0.856	0.479	-0.068	0.892	0.381	0.024	0.145
Y	0.913	0.367	-0.096	0.894	0.345	-0.198	-0.097
Th	0.246	0.791	-0.200	0.011	0.136	0.838	0.165
U	0.201	0.949	-0.073	0.685	-0.326	0.431	-0.168

of significant correlation. Furthermore, Sn was strongly positively correlated with W, as the numbers obtained were close to + 1, while heavy REEs (HREEs) had a moderate positive correlation with Th and U.

The application of the multivariate processing method, based on the distribution of elemental content in the weathering sample, produced 4 components according to correlation values close to 1.0. These components were grouped as follows: HREEs, Y, and U positively correlated (component 1), light REEs (LREEs) and HREEs were positively correlated (component 2), LREEs and Th groups were positively correlated (component 3), including the Sn and W groups were positively correlated (component 4), as presented in Table 5. Based on the results, it was observed that Sn was not correlated with REEs in the weathering samples.

## DISCUSSION

The statistical analysis of Sn-REEs content data from granite, quartz veins, and weathered granite samples showed a weak negative correlation. This was inconsistent with REEs resources, including monazite, xenotime, and zircon, which always spatially correlated with Sn minerals (cassiterite) in alluvial deposits or as tin by-products. This showed that the statistical approach did not support the genetic relationship between Sn and REEs. In contrast, Sn and W, U, and Th were positively correlated, while HREE had a partial correlation with Th and U.

The presence of REEs in the form of monazite and zircon (REE minerals) was observed in thin sections, as shown in Figure 2. In the polished section, Sn in the form of stannite was observed along with Cu (chalcopyrite) in granite, as presented in Figure 3. The presence of stannite showed the formation of primary tin, namely the early magma crystallization stage, showing a primary genetic relationship between REEs and Sn as inclusions in granite. From the observations on the polished section, Sn (stannite) and Cu (chalcopyrite) showed intergrowths. This phenomenon indicated the genetic relationship between Sn and REEs represented in the granite sample TBL-21MN/02B/R Toboali, which was in the same formation phase. Furthermore, stannite in a chemical formulation was found to contain elements of Cu composing  $\text{Cu}_2\text{FeSnS}_4$ .

The presence of xenotime (REEs (Y)) in the granite host rock sample (TBL-21MN/09A/R) was confirmed in BSE images, as shown in Figure 7C. However, xenotime was absent in quartz veins as late-stage hydrothermal failed to introduce Y and could persist alongside magmatic-hydrothermal during the evolving process. This phenomenon showed that there was no significant correlation between Sn and REEs.

The occurrence of quartz veins was intensively near the contact area between metamorphic rocks of the Pemali Formation and granite of Klabat Granite in Air Gegas and hence enriched with cassiterite, as shown in Figures 6 and 8.

However, the presence of cassiterite does not coincide with REEs, compared to granite as the host rock in Toboali (TBL-21MN/09A/R) containing xenotime inclusions in biotite. In this rock, Sn and REEs are in the same parental granite as for xenotime, which was formed primarily from magmatic solutions along with the crystallization of biotite (rock-forming minerals). Monazite and xenotime were also formed in the initial crystallization stage of magma, by reacting with apatite crystals and dissolved fluid, hydrothermal processes, as well as metasomatism infills pores and fractures in apatite of granite (Harlov, 2015). Based on the results, quartz veins were deposited from the late-stage hydrothermal solution in granite (sample TBL-21MN/09B/R), which was enriched in Sn but was depleted in REEs. Furthermore, granite presented in Figure 7 contained Y, showing the absence of correlation between Sn and REEs.

In the BSE image of a quartz vein hosted in granite at TBL-21MN/05E/R, cassiterite was observed. The results of SEM-EDS mapping on cassiterite spots 2 and 4 showed Sn 72.62-75.92%, Pr 5.75%, and Pm 7.28% weight units. These values are relatively high, indicating that the magmatic solution brought HREE elements along with Sn. The contents of W, Th, and U were also significant, while chalcopyrite (Cu), sphalerite (Zn), and thorite (Th) were present as inclusions in biotite confirmed on the BSE image, as shown in Figure 6. The presence of single-phase Sn and Cu adjacent to quartz vein-bearing granite (TBL-21MN/14/R) in Air Gegas was also confirmed in BSE images, as presented in Figure 8D. Based on Figure 7, Ti (rutile) and Sn (cassiterite) were found in the sample of quartz vein hosted in granite (TBL-21MN/09B/R), Toboali.

The results obtained showed that the mineralizing fluid containing Sn, W, Cu, Zn, Ti, and REEs originated from magmatic gas in a deep magma chamber, increasing to shallow depths through the fault structure as a "channel way". In this context, it was suggested that the lateral structure in Air Gegas, as shown in the published geological map of South Bangka (Mangga & Djamal, 1994; Margono *et al.*, 1995), acted as an outlet for hydrothermal solutions. These structural markings were observed on the mining wall of the TBL-21MN/14/R sample location, Air Gegas.

During the formation of the Klabat granite pluton, quartz veins were formed due to post-magmatic hydrothermal solution deposition infilling the fractures in granite and metamorphic rocks (Pemali Formation). In this zone, the deposition of REEs, Sn, Cu, Zn, Th, and other elements occurred at lower temperature conditions. This showed the final stage of deposition of a hydrothermal solution (quartz vein) hosted in granite, as confirmed on the BSE image and detected by SEM-EDS mapping results. At this stage, the enrichment of cassiterite was formed as the target of local miners, particularly in weathered areas. The presence of cassiterite in the weathering of tin-bearing granite was confirmed by XRD analysis, showing Sn of stannite cassiterite, as shown in Table 2.



In a previous fluid inclusion study, tin was found to be deposited at low temperatures (210-220°C) and salinity (5-6 wt. % NaCl eq) (Shita & Lucas, 2009). The temperature of the hydrothermal solution in forming cassiterite was also found at an interval of 250-450°C (Faiz *et al.*, 2019), allowing gradual phases of deposition through evolving processes. Tourmaline observed in sample TBL-21MN/14/V presented in Figure 5A shows the evolved magmatic-hydrothermal (Yang *et al.*, 2015). Moreover, the differentiation and evolution of granite can lead to an increase in the content of Sn and W, compared to REEs which decreased as accessories in the Nanling region, South China (Hua *et al.*, 2007). In South Bangka, the Sn content in quartz veins increased as a late-stage hydrothermal product. Due to the different deposition stages, the Sn-REE composition values of all samples were not statistically correlated.

### CONCLUSION

In conclusion, this study showed the presence of Sn and REEs in placer deposits in the form of cassiterite (Sn), monazite, xenotime, and zircon (REEs). Spatial analysis confirmed that Sn and REEs were found in granite, quartz vein, and weathering samples, suggesting a genetic relationship. Based on mineralogy and SEM data, it was discovered that both elements originated from the same magmatic fluid sources with different formation stages. REEs, Sn, and metal sulfides were observed to have been formed during early magmatic crystallization. During the evolving process, Sn as cassiterite formed in late-stage hydrothermal. The Pearson coefficient calculation results and statistical multivariate approaches showed no correlation between Sn and REEs in granite, quartz vein, and weathering samples. This absence of correlation was attributed to genetic relations influenced by various physical-chemical conditions in the different deposition stages. Moreover, the genetic relationship of Sn-REEs still required further investigation to ensure the accuracy of results.

### ACKNOWLEDGEMENT

The authors are grateful to the Director-General of Mineral and Coal of Indonesia for funding the REEs inventory project 2021 and the head of the Centre for Mining Technology Development. Furthermore, the authors are grateful to the head of the Centre for Mineral Coal and Geothermal Resources for appointing Armin Tampubolon as a team coordinator and allowing the use of data analyses, including the local porters who assisted during fieldwork. The authors also thanks the reviewers for their input in improving the manuscript

### AUTHOR CONTRIBUTIONS

AT is the main contributor to conducting the investigation, data analysis, validation, interpretation, and writing original manuscript. IS, MFR, and ETY contributed to research design, geology conception, writing review, discussion, and editing.

### CONFLICT OF INTEREST

None of the authors have a conflict of interest in regard to this research or its funding

### REFERENCES

- Abidin, H.Z., 1999. Toboali Alluvial Tin Deposit: Geology, depositional processes, and material sources. In: Baharuddin & Surawardi (Eds.), *Metallogeni Sundaland Vol I. Indonesia Mining Journal*, 1-12.
- Abidin, H.Z., 2014. Toboali Alluvial Tin Deposit: Geology, depositional processes, and material sources. In: Baharuddin & Surawardi (Eds.), *Metallogeni Sundaland Vol I. Geological Agency of Indonesia*, 137-150.
- Camilla, L.O., Geoffrey, R.N., Kathryn, H., Robert, S.F., Corby, G.A., & Frances, W., 2019. Apatite enrichment by rare earth elements: A review of the effects of surface properties. *Advances in Colloid and Interface Science*, 265, 14–28.
- Chengyu, W.U., 2008. Bayan Obo Controversy: Carbonatites versus Iron Oxide-Cu-Au-(REES-U). *Resource Geology*, 58(4), 348 – 354.
- Cobbing, E.J., Pitfield, P.E.J., Darbyshire, D.P.F. & Mallick, D.I.J., 1992. The Granites of the South-East Asian Tin Belt. *Overseas Memoir 10, British Geological Survey*. 369 p.
- Crow, M.J. & Van Leeuwen, T.M., 2005. *Metallic mineral deposits. Geological Society London Memoirs*, 31, 147-174.
- Faiz, A.P., Syarifuddin, M., Angger, I.A., Faric, R.S., Angga, W.Y. & Reza A., 2019. Structure System and It Controls to Mineralization of Primary Tin Deposit, Airdibi Area, Jebus Subdistrict, West Bangka, Bangka and Belitung. *Journal of Physics: Conference Series*, 1363.
- Franco, P., 1992. *Hydrothermal Mineral Deposits: Principles and Fundamental Concepts for the Exploration Geologists*. Springer-Verlag, US. 709 p.
- Franto, Subagyo, P. & Lucas, D.S., 2019. The Study of Hydrothermal Alteration and Type Study of Primary Tin Mineralization in Tsk. Pengarem, Southern Bangka Island. *IOP Conf. Series: Earth and Environmental Science*, 375, 012008.
- George, J.S., Carlee, A. & Suzanne, P., 2015. Which materials are 'critical' and 'strategic'. In: Simandl, G.J. & Neetz, M., (Eds.), *Symposium on Strategic and Critical Materials Proceedings*, November 13-14, 2015, Victoria, British Columbia. *Geological Survey Paper 2015-3*, 1-4.
- Harlov, D.E., 2015. Apatite: A fingerprint for metasomatic processes. *Elements*, 11(3), 171-176. <https://doi.org/10.2113/gselements.11.3.171>.
- Hua, R.M., Zhang, W.L., Gu, S.Y., & Chen, P.R., 2007. Comparison between REES granite and W-Sn granite in the Nanling region, South China, and their mineralizations. *Acta Petrologica Sinica*, 23(10), 2321-2328.
- Hutchison, C.S., 2014. Tectonic evolution of Southeast Asia. *Bulletin of the Geological Society of Malaysia*, 60, 1-18.
- Kurnia, S.W. & Priadi, B., 2013. Petrography and Geochemical Major Element of Granite, Bangka Island: Initial Evaluation of Tektonomagmatisme. *Eksplorium*, 34, 2, 1–16. (in Indonesian)
- Kurniawan, A., 2014. *Geology of Granitoid Rocks in Indonesia and Their Distributions (in Indonesian)*. Masyarakat Ilmu Bumi Indonesia (Indonesian Geography Society), 1/E-3. 16 p.
- Liu, L., Hu, R.Z., Zhong, H., Yang, J.H., Kang, L.F., Zhang, X.C., Fu, Y.Z., Mao, W., & Tang, Y.W., 2020. Petrogenesis of multistage S-type granites from the Malay Peninsula in the Southeast Asian

- tin belt and their relationship to Tethyan evolution. *Gondwana Research*, 84, 20-37. <https://doi.org/10.1016/j.gr.2020.02.013>.
- Mangga, S.A., & Djamal, B., 1994. Geologic Map of North Bangka Quadrangle, Scale 1: 250,000. Geological Research and Development Centre.
- Margono, U., Supandjonom, E. & Partoyo, E., 1995. Geologic Map of South Bangka Quadrangle, Scale 1: 250,000. Bandung. Geological Research and Development Centre.
- Marker, H.J. Dirk, 2013. Perbedaan Genesa Magma antara Tin Bearing Granitoid Rocks dari Jalur Kepulauan Timah Indonesia dan Tin Barren Granitoid Rocks Dari Pulau Bintan. *Jurnal Sumber Daya Geologi*, 23(2), 81-92.
- Murakami, H. & Ishihara, S., 2008. Fractionated Ilmenite series Granites in Southwest Japan: Source Magma for REES-Sn-W Mineralizations. *Resources Geology*, 56(6), 245-256.
- Ng, S.W.P., Martin, J.W., Whitehouse, M. J., Muhammad H. Roselee, M.H., Claudia, T., Sayed, M., Grahame, J.H.O., Azman, A.G. & Su-Chin, C., 2017. Late Triassic granites from Bangka, Indonesia: A continuation of the Main Range granite province of the South-East Asian Tin Belt. *Journal of Asian Earth Sciences*, 138, 548–561.
- Reza, M.F., Trisa, M., Rudy, G., Tampubolon, A., Prima, M., & Kisman, 2018. Potential Evaluation of REES in South Bangka Regency, Bangka Belitung Islands Province, in related to Tin Deposits. Centre for Mineral Coal and Geothermal Resources (unpublished) (in Indonesian).
- Shita, K., & Lucas, D.S., 2009. Characteristics of granitic rocks of Bangka Island, Indonesia, and their associated mineralization. Thesis S2 Teknik Geologi, UGM. (unpublished).
- Schwartz, M.O. & Surjono, 1991. The Pemali tin deposit, Bangka, Indonesia. *Mineral Deposita*, 26, 18- 25.
- Schwartz, M.O., Rajah, S.S., Askury, A.K., Putthapiban, P. & Djaswadi, S., 1995. The Southeast Asian Tin Belt. *Earth-Science Reviews*, 38, 95-293.
- Soetopo, 2013. Studi Geologi dan Logam Tanah Jarang (REES) Daerah Air Gegas, Bangka Selatan, *Eksplorium*, 34(1), 51-62.
- Tampubolon, A., Syafri, I., Rosana, M.F., & Yuningsih, E.T., 2022. The occurrence of primary REE minerals and their paragenesis within S-type granite and quartz veins, South Bangka, Bangka Belitung Islands, Indonesia (preprint). <https://doi.org/10.21203/rs.3.rs-1849349/v1>.
- Weng, Z.H., Gavin, M.M., Simon, M.J. & Nawshad, H., 2017. Assessment of Global Rare Earth Supply & Wind Energy Growth: Opportunities and Challenges, *GREESn and Sustainable Chemistry Conference*, Berlin, Germany, 4-17<sup>th</sup> May.
- Weng, Z.H., Jowitt, S.M., Mudd, G.M. & Haque, N., 2013. Assessing rare earth element mineral deposit types and links to environmental impact, *Journal Applied Earth Science*, 122, 83-107.
- Yang, S.Y., Jiang S.Y., Zhao, K.D., Dai, B.Z., & Yang, T., 2015. Tourmaline as a recorder of magmatic–hydrothermal evolution: An in situ major and trace element analysis of tourmaline from the Qitianling batholith, South China. *Contribution Mineral. Petrology*, 170, article 42. <https://doi.org/10.1007/s00410-015-1195-7>.
- Zglinicki, K., Szamalek, K., & Wołkiewicz, S., 2021. Critical Minerals from Post-Processing Tailing. A Case Study from Bangka Island, Indonesia. *Minerals*, 11(4), 352. <https://doi.org/10.3390/min11040352>.

*Manuscript received 17 August 2023;  
Received in revised form 13 October 2023;  
Accepted 26 December 2023  
Available online 30 May 2024*